

Full length article

Characterization and modeling of oxides precipitation in ferritic steels during fast non-isothermal consolidation



X. Boulnat ^{a, b, *}, M. Perez ^{b, **}, D. Fabrègue ^b, S. Cazottes ^b, Y. de Carlan ^a

^a CEA, DEN, Service de Recherches Métallurgiques Appliquées, F91191 Gif-sur-Yvette, France

^b Université de Lyon, INSA-Lyon, MATEIS UMR CNRS 5510, F69621 Villeurbanne, France

ARTICLE INFO

Article history:

Received 11 March 2015

Received in revised form

30 December 2015

Accepted 16 January 2016

Available online xxx

Keywords:

ODS steels

Precipitation modeling

Nucleation

Nanoparticles

Atom-probe tomography

TEM

ABSTRACT

The precipitation behavior of nanosized binary Y_2O_3 and complex $Y_2Ti_2O_7$ precipitates in oxide-dispersion strengthened ferritic steels was modeled by a nucleation, growth and coarsening thermodynamic approach. Focus was made on non-isothermal treatments that simulate typical consolidation processes of nanostructured steels. In order to assess the model for fast non-isothermal treatments, a field-assisted consolidation process was used. The precipitation state was characterized at nanoscale by transmission electron microscopy, small-angle neutron scattering and atom-probe tomography. Both simulation and experimental results demonstrated the following precipitation mechanisms: (i) rapid nucleation of both Y_2O_3 and $Y_2Ti_2O_7$ during the heating stage (ii) limited growth and coarsening of nanoclusters during soaking time and further annealing at high temperature (1100 °C). A new coefficient diffusion of yttrium in ferrite was proposed to assess the thermal stability of nano-oxides.

© 2016 Acta Materialia Inc. Published by Elsevier Ltd. All rights reserved.

1. Introduction

Oxide-Dispersion Strengthened (ODS) ferritic steels have been widely developed these recent years for high temperature applications. Processed by powder metallurgy, these materials are usually produced by hot isostatic pressing (HIP), hot extrusion, or more recently by Spark Plasma Sintering technique (SPS) [1–5]. They owe their good high-temperature mechanical properties to a fine dispersion of nanosized oxides that act as efficient obstacles for dislocations and grain boundaries. Depending upon the chemical composition and the consolidation technique and parameters, various kinds of oxides have been reported in the literature. The most common are yttrium oxides Y_2O_3 and ternary oxides $Y_2Ti_2O_7$. The latter were observed to enhance tensile strength and creep resistance due to an increased number density and a lower mean radius of the precipitated particles. They have been the subject of numerous characterization studies at the nanoscale, including transmission electron microscopy [6–8], small-angle neutron scattering [9–11] and more recently atom-probe tomography [12].

What is widely recognized is that these nanoparticles exhibit an extraordinary thermal stability [13], even at temperatures close to the solidus of the ferritic matrix. Thanks to an observation at the atomic scale, this coarsening resistance was linked to the large amount of oxygen vacancies ($\approx 10\%$) that could stabilize the clusters [14]. However, another study by Ribis and de Carlan demonstrated that the morphology of the particles $Y_2Ti_2O_7$ evolved upon heating in order to minimize their energy within the system [15]. The shape transition from spherical to cubical geometry was described as a way to reduce the elastic distortion created at the interfaces. Thus, the elastic energy governed by the misfit between the precipitates and the matrix can influence the precipitation of these fine particles. Whether the coarsening resistance is only of thermokinetic nature (slow diffusion of yttrium) or related to more complex phenomena is still questioned.

Most studies were made on extruded or HIPed materials with stabilized precipitation. Hence, a few data is available on the early stage of precipitation, specially on the nucleation behavior of these particles. Since the particles are nanosized, the characterization can be tedious, expensive and sometimes subject to controversy. Experimental tools are limited when dealing with the nucleation kinetics during non-isothermal treatments, which are representative of the consolidation processes of ODS steels. In this context, modeling tools are excellent means to understand the precipitation

* Corresponding author.

** Corresponding author.

E-mail addresses: boulnat.xavier@gmail.com (X. Boulnat), michel.perez@insa-lyon.fr (M. Perez).

mechanisms. For instance, the role of yttrium diffusion or the influence of the elastic misfit during nucleation and further growth and coarsening are still debatable. Various models can be used to simulate the solid-state precipitation in metallic materials. Readers are referred to [16] for an elaborate review of solid-state precipitation theories and associated calculation algorithms. Three main categories are distinct and complementary. First of all, the predictive models like DFT (density functional theory) or Monte Carlo tend to determine analytically the behavior of the material at the atomic scale [17,18]. Then, semi-predictive models combining thermodynamic and diffusion databases can model solid-state precipitation in multi-components systems [19]. Finally, JMAK-type (Johnson-Mehl-Avrami-Kolmogorov) mathematical formalisms allow to describe phase transformation kinetics using both physical and arbitrary coefficients. These different kinds of model involve complementary time and space scales. JMAK models encounter difficulties to reproduce non-isothermal treatments and physical mechanisms [20]. At the opposite, atomistic models are powerful tools to understand physical mechanisms but the time scale is reduced to approximately 10^{-6} s and involve very long time calculation for a limited number of atoms [21,22]. For precipitation, a good compromise consists of thermokinetic model using the nucleation, growth and coarsening theories [23,24].

Classic thermodynamic modeling consists in calculating the driving force of the formation of a possible compound (phase) from a supersaturated solid solution. In ODS steels, some controversial studies lead to contradictory conclusions on whether yttrium, oxygen atoms transform into a solid solution in the iron matrix. Indeed, mechanical alloying involves far-from-equilibrium mass transport, local heating, cold welding and other mechanisms that are difficult to model [25]. From recent atom-probe tomography, clustering of yttrium and titanium-rich particles was observed after a certain milling time [12,26,27]. This is not surprising since perfect solid solution is always difficult to achieve, especially for highly non soluble elements. However, the community mainly agrees with the fact that these subnanometric clusters are quite homogeneously distributed in the powders. Also, after annealing or consolidation at high temperature, the clusters tend to crystallize and form stoichiometric phases [7,15,14,28]. Thus, the starting point before high-temperature consolidation still deals with the need of diffusion-governed atoms transport to form well-defined, crystalline precipitates. In this sense, this study applies a diffusion-based precipitation model using the nucleation, growth and coarsening theory.

The assessment of this model is based on:

- (i) the validation of the numerical model thanks to the case study of unique phase Y_2O_3 .
- (ii) Then, the precipitation of complex $Y_2Ti_2O_7$ is studied in ODS steels containing yttrium, titanium and oxygen. The numerical results are compared to SANS data after Alinger et al. [29,30].
- (iii) Finally, this model is applied to rapid non-isothermal treatments using field-assisted consolidation process. These results are compared to experimental data collected in the present study by Small Angle Neutron Scattering (SANS), Transmission Electron Microscopy (TEM) and Atom-Probe Tomography (APT).

2. Material and methods

2.1. Materials

A powder of high-chromium ferritic steel was produced by ingot

gas atomization by Aubert&Duval. The powder particles were then mechanically alloyed with submicronic yttria powder (Y_2O_3) using a high-energy attritor by Plansee SE. Milling conditions and microscopic evaluation of the as-milled powder are recalled in Ref. [9]. Using Focused Ion Beam (FIB) cross-sectioning of powder particles, the nanostructure was investigated by scanning electron microscopy (SEM) and Electron Back Scatter Diffraction (EBSD). Most of the grains are highly deformed and the smallest nanosized grains are not indexed due to a huge amount of dislocations, roughly estimated by Kernel Average Misorientation as over $1 \times 10^{16} m^{-2}$.

The chemical composition of the milled powder is reported in Table 1. This powder is representative of common industrial nanocrystalline powder widely used to process nanostructured materials. In this particular alloy, yttrium, titanium and oxygen are expected to form nanoparticles during hot processing.

2.2. Characterization methods

Transmission Electron Microscopy (TEM) characterization was performed on an apparatus TEM JEOL 2010F equipped with an Energy Dispersive X-Ray Spectroscopy (EDX) XMAX 80 for chemical analysis. The thin foils were prepared using the following method: (i) Mechanical polishing to get a final thickness between 60 and 90 μm (ii) 3-mm disk stamping and further polishing with diamond paste up to 3 μm (iii) Electrolytic etching with a solution composed of 70% of ethanol, 20% ethylene glycol monobutyl ether and 10% of perchloric acid and cooled to 0 °C (iv) Ionic polishing to eliminate eventual oxidation before observation. The apparatus was a PIPS (Precision Ion Polishing System) from Gatan equipped with a double ion gas gun polishing the surface with an incident angle from -10 to 10° . Gun energy was set at 4.2 keV with a magnitude of 20 A.

SANS experiments were performed at the Laboratoire Léon Brillouin CEA Saclay, using the PAXY small angle scattering spectrometer for high resolution in q -space, under strong magnetic field (1.7 T). As mentioned in Refs. [31], a magnetic field of magnitude 1.2 T is sufficient to separate the magnetic and nuclear contributions. SANS experiments were set to determine the distribution of particles smaller than 15 nm in radius. This corresponds to a scattering vector q between 0.1 and 1.6 nm^{-1} . This was obtained by selecting neutron wavelengths of 0.6 and 1 nm ($\pm 10\%$ due to monochromator dispersion) and a distance between sample and detector of 2 and 5 m, respectively. A 2D detector with area $64 \times 64 cm^2$ was used to collect scattered neutrons. As detailed in Refs. [11], a direct modeling was used in the current study. The scattering function was calculated for a given distribution of nano-scatterers and compared to the experimental function. A least squares method was used to obtain the best fitting parameters. The particles were assumed spherical - even some can have cuboidal or ellipsoidal shapes [15] - and of constant chemical composition. Particle mean radius r_m of the scattering population was calculated assuming a normalized number density function of radii $h(r)$. Given these assumptions, one can write the scattering intensity as:

$$I(q, r) = \Delta\rho^2 N_p V_p^2 F_{sph}(q, r) S(q, r) \quad (1)$$

where N_p is the scatterers density, V_p the volume of a scattering

Table 1
Mean Composition (in wt%) of the milled powder.

Fe	Cr	W	Y	O	Ti	C
bal.	13.9	1.0	0.16	0.15	0.32	0.04

particle, $\Delta\rho$ the variation in diffusion length densities between the matrix and the scatterers. $F_{sph}(q,r)$ is the shape factor for spheres:

$$F_{sph}(q,r) = \frac{3[\sin(qr) - qr \cos(qr)]^2}{(qr)^3}$$

$S(q,r)$ is the structure factor resulting from the particles interaction. If the volume fraction of precipitates is observed to be less than 1% (diluted system), $S(q,r)$ tends to 1. A Gaussian distribution of spherical particles was chosen for direct modeling:

$$h(R) = \frac{1}{\sigma\sqrt{2\pi}} \frac{e^{-(r-r_m)^2}}{2\sigma^2} \quad (2)$$

Considering that the matrix is ferromagnetic, one can verify the global chemical composition of the nano-scattering particles by decoupling the nuclear and magnetic contrasts [30,11]. Indeed, the scattering ratio A is given by:

$$A = 1 + \frac{\Delta\rho_M^2}{\Delta\rho_N} \quad (3)$$

where $\Delta\rho_M$ and $\Delta\rho_N$ are the magnetic and nuclear contrasts, respectively. Regarding ODS steels, the ratio A depends upon the composition of the steel and the nature of the oxides. In Fe–14Cr steel, typical values are 2.5 for pyrochloric structure $Y_2Ti_2O_7$ and 3.2 for cubic Y_2O_3 , as demonstrated in Ref. [11].

Atom Probe Tomography samples were prepared using the lift-out method with a FEI Helios microscope equipped with a Focused Ion Beam. The APT analyses were carried out on a IMAGO LEAP 3000 XHR, with laser or electric pulses. Analyses were realised at 50 K, with a pulse fraction of 20%, with a laser energy of 0.4 nJ at a pulse rate of 200 kHz.

3. Experimental results

3.1. Transmission electron microscopy (TEM)

The microstructure of the consolidated material at 850 °C is reported in Fig. 1. The material presents a bimodal distribution of grain sizes, with several micrometer large grains surrounded by ultrafine grained regions with grains with a diameter down to 50 nm. Since these ultrafine grains (UFGs) contain numerous dislocations, they originate from the initial deformed nanostructure and cannot be small recrystallized grains. Dislocation density is still very high and dislocations walls are visible within the grains (see Fig. 1)(b).

At this stage, nanosized precipitates were observed in both UFG and large grains, with diameter ranging from 2 to 4 nm (Fig. 2(a)). The size distribution was determined in the coarse grain visible in Fig. 1(a) based on more than 100 particles. A mean radius of 1.2 nm was found, which is consistent with SANS data (mean radius 1.4 nm), see Fig. 3.

However, their chemical and structural characterization was difficult due to their small size and only a few number of them could be identified. Specially, the large precipitate of Fig. 2(b) was indexed as a $Y_2Ti_2O_7$ precipitate. This is the first evidence of rapid nucleation of nanocrystalline $Y_2Ti_2O_7$ during fast non-isothermal consolidation, including SPS.

Fig. 4 presents a large spherical Y_2O_3 precipitate, with a diameter of 85 nm, with parallel facets on two sides. It seems that its shape transforms from spherical to cuboidal, as predicted by Ribis and de Carlan, for smaller precipitate size. The facets are parallel to the $\langle 200 \rangle$ direction of the precipitates and 10° disoriented to the $\langle 110 \rangle$ direction of the matrix. These results confirm that the

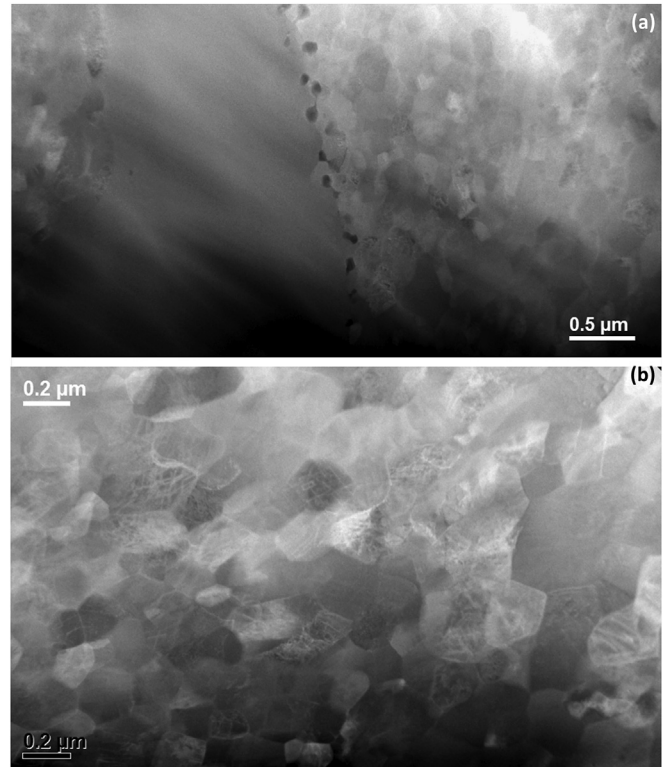


Fig. 1. (a) General view of the microstructure of the 850 °C consolidated sample, with the presence of very large grains and (b) Ultra fine grained regions, where a high dislocation density is visible in the grains.

morphological change of the nanosized particles most likely accounts for the minimization of the elastic strain energy during coarsening but also demonstrate that this mechanism occurs much earlier than ever observed: the cuboidal geometry is partially effective after rapid consolidation at 850 °C for few minutes, whereas Ribis observed this kind of shape after annealing at 1300 °C for few hours. This morphological variation depends on the type and the size of the precipitate. For example, in the generalized broken-bond approach (GBB) [32], a size correction can be applied to the interfacial energy:

$$\gamma(r) = \alpha(r) \times \gamma_0 \quad (4)$$

where $\alpha(r)$ is a size-correction function that - at constant chemical composition - only depends on the radius of the precipitate [33].

After consolidation at 1100 °C, no significant changes were observed in the microstructure; a bimodal distribution of grain size is still present, as well as the presence of 'coarse' oxides at grain boundaries together with nanosized precipitates within the grains. The 'coarse' precipitates are mainly titanium oxides, with diameter ranging from 50 to 80 nm. A complete multiscale characterization, including the quantification of the coarse precipitation, will be presented elsewhere.

Focus is here only made on nanosized precipitation. Since it is of prime importance to verify whether the particles distribution is homogeneous within the microstructure, TEM characterization was performed in both coarse grains and ultrafined grains. Evidence of precipitates located at dislocations are presented in Fig. 5.

An attempt to quantify the nanoparticles number density is reported in Fig. 6. Number densities were calculated from the formula $N_p = N/V$, with N_p the number density of precipitates, N the number of precipitates on the 2D TEM micrograph and V the local

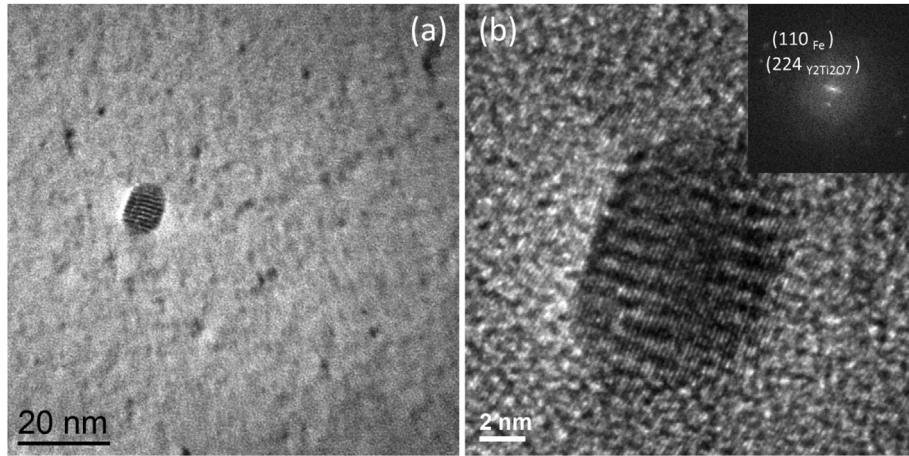


Fig. 2. (a) TEM micrograph acquired in g200 to beam conditions revealing the presence of nanosized precipitates in the 850 °C consolidated sample. (b) Enlarged view of the larger precipitate, of $Y_2Ti_2O_7$ type.

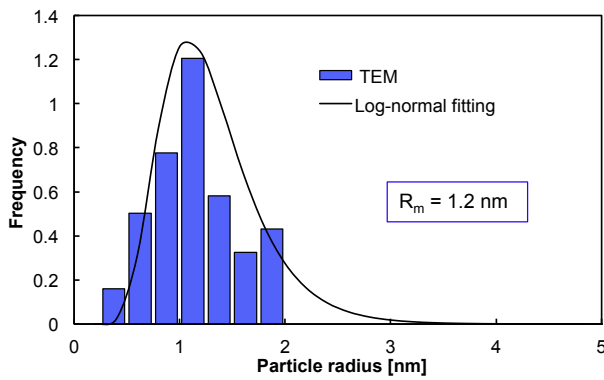


Fig. 3. Experimental TEM particles size distribution in ODS SPSeD at 850 °C fitted by a log normal distribution.

volume of the foil. The thickness of the foil was determined using thickness fringes in two-beam mode. Extinction conditions are related to the local thickness and to the orientation of the grain, through the tabulated extinction distance ξ_g [34]. Although the representativeness of these measurements are debatable, the size

distributions are quite similar in ultrafine and coarse grains. Lots of dislocations were found in the grains, interacting with precipitates. Thus, heterogeneous nucleation on dislocations is highly probable. The rapid precipitation of populous nanoparticles is most likely a key factor of the limited dislocation annihilation. Somehow, the synergistic combination between high dislocation density and high density of particles enhances the stability of this metallurgical state.

Fine particles were detected all over the grains by High-Resolution TEM (HRTEM) or in two beam conditions. Indeed, the coherent character of the particles makes it difficult to visualize these nanoscale precipitates in conventional mode. When observing in two beam mode (Fig. 7), the misfit between precipitates and matrix generates so-called Moiré fringes [15].

The distance between the fringes can be related to the inter-planar distance of the planes generating the fringes with the following relationship:

$$D^{fr} = \frac{d_p \cdot d_m}{|d_p - d_m|} \tag{5}$$

where d_p and d_m are the inter-reticular distance of the precipitate and the matrix, respectively.

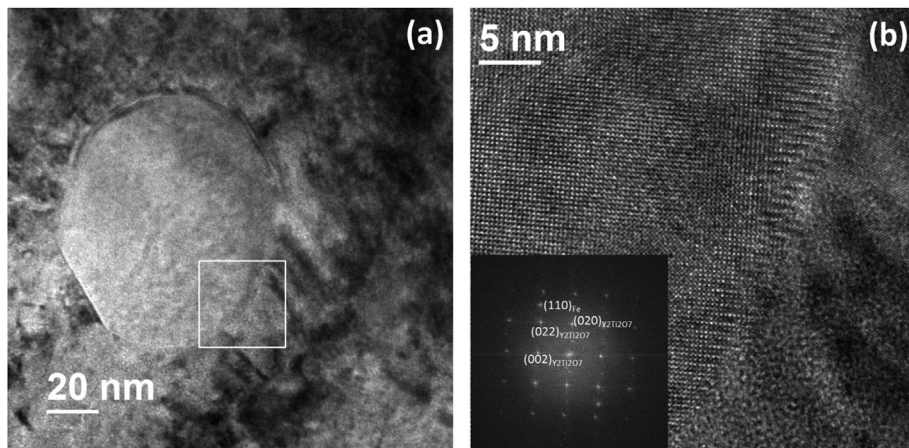


Fig. 4. (a) Large Y_2O_3 precipitate observed in the 850 °C consolidated sample. Parallel facets indicate that the precipitate morphology evolves from spherical to cuboidal. (b) Wiener Filtered HRTEM micrograph of the interface between the precipitate and the matrix.

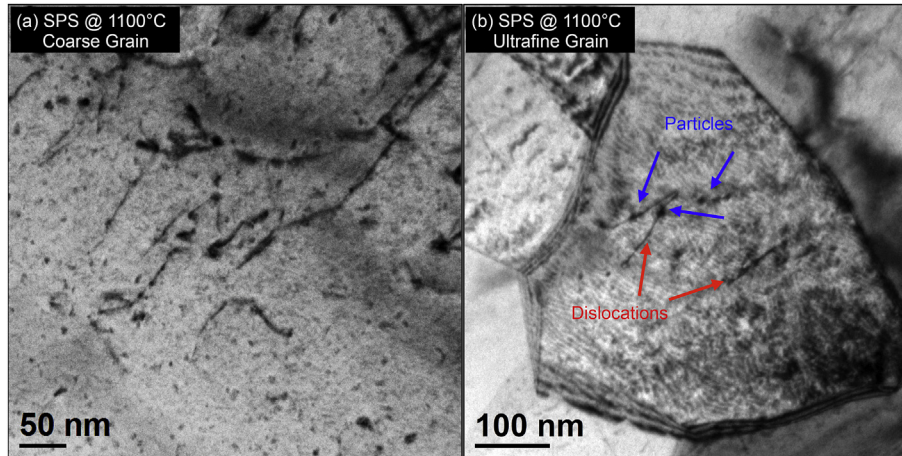


Fig. 5. (a) Nanoparticles in a coarse grain and interacting with dislocations (b) TEM image on nanoparticles in ultrafine grains. Some of these are also located on dislocations.

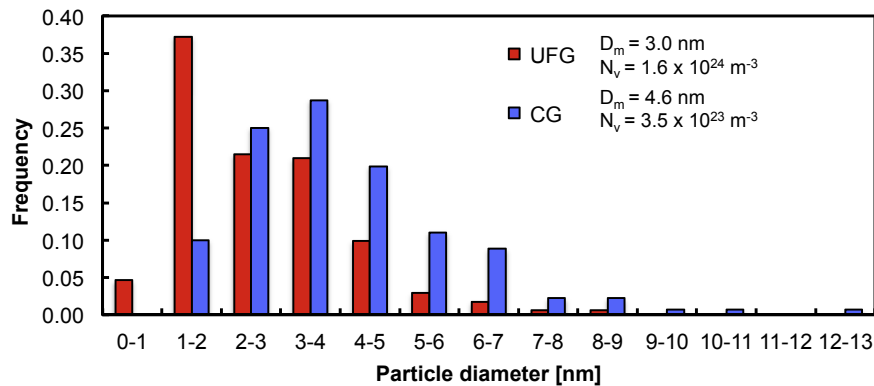


Fig. 6. Precipitate size distribution measured in ultrafine grains (UFG) and coarse grains (CG) of the ODS steel SPSed at 1100 °C. The estimated uncertainty on the number density is 10^{23} m^{-3} .

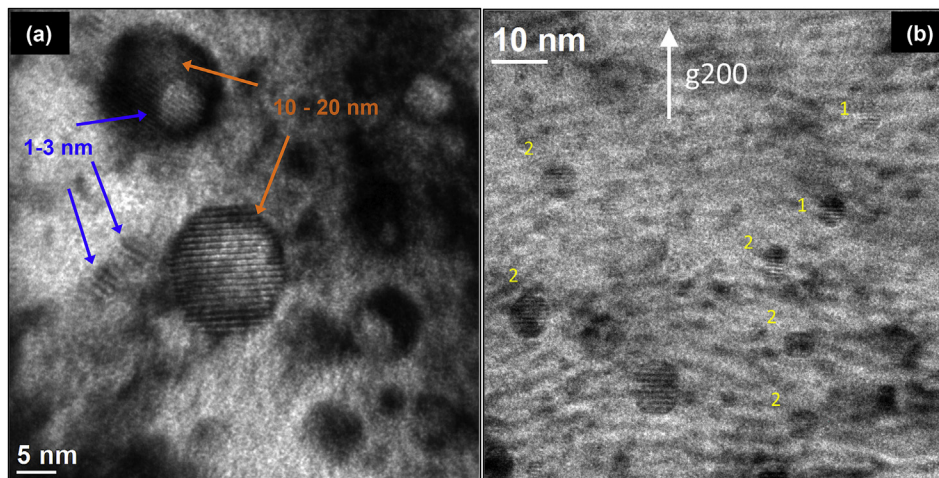


Fig. 7. (a) Nanoparticles observed in two beam conditions in the 1100 °C annealed sample. In (b), precipitates numbered 1 are fcc Y_2O_3 whereas precipitates numbered 2 are fcc $\text{Y}_2\text{Ti}_2\text{O}_7$.

Fig. 7 presents different kind of precipitates observed in the sample annealed at 1100 °C for 16 h. Both coherent Y_2O_3 and $\text{Y}_2\text{Ti}_2\text{O}_7$ were identified. On Fig. 8(a), two cuboidal fcc precipitates were evidenced presenting the following OR1 with the matrix:

$$\{100\}_{Fe} \parallel \{100\}_{fcc} \text{ and } \langle 100 \rangle_{Fe} \parallel \langle 100 \rangle_{fcc}$$

fcc being $\text{Y}_2\text{Ti}_2\text{O}_7$ or Y_2O_3 . The lattice parameters of $\text{Y}_2\text{Ti}_2\text{O}_7$ and Y_2O_3 bcc phase are too close to strictly distinguish between the two

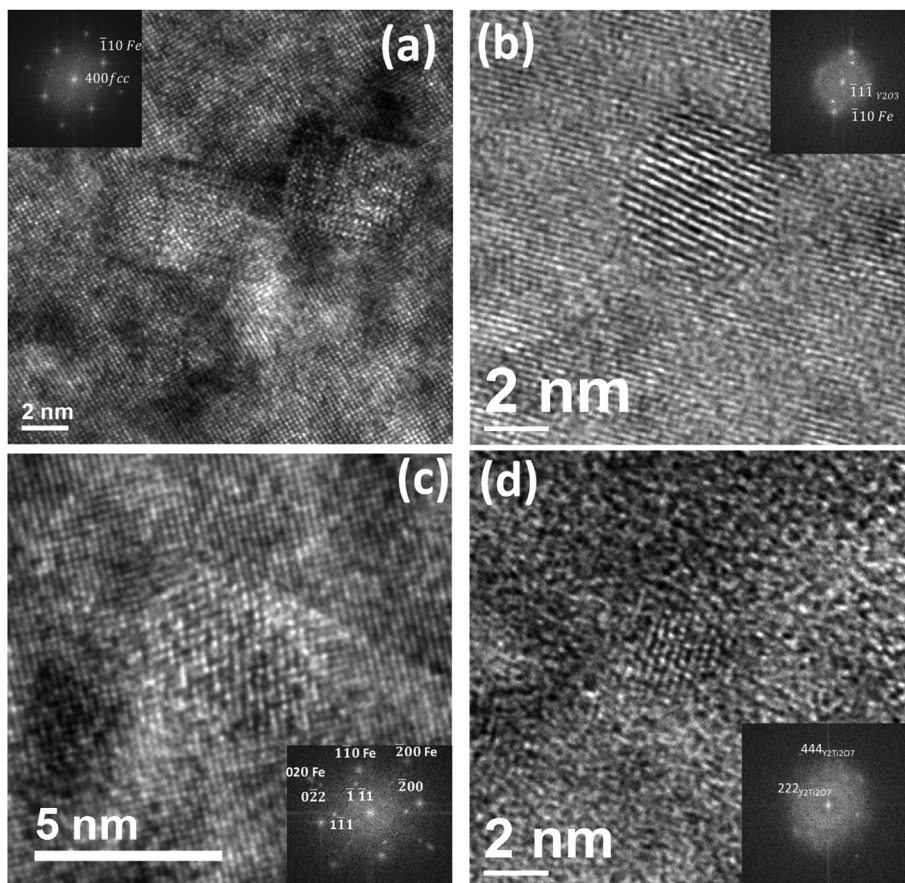


Fig. 8. Nanoprecipitates observed in the 1100 °C annealed sample: (a) 5–7 nm cuboidal fcc precipitates of Y_2O_3 or $Y_2Ti_2O_7$ type in OR1 with the matrix, (b) Y_2O_3 precipitate presenting OR2 relative to the matrix, (c) $Y_2Ti_2O_7$ precipitate presenting a cube-on-cube OR with the matrix, (d) 2.5 nm diameter $Y_2Ti_2O_7$ precipitate.

phases.

Fig. 8(b) illustrates a fcc Y_2O_3 precipitate observed in $(110)_{Fe}$ two beam conditions, which presents the following OR2 with the matrix:

$$\{001\}_{Fe} \parallel \{001\}_{Y_2O_3} \text{ and } \langle 110 \rangle_{Fe} \parallel \langle 110 \rangle_{Y_2O_3}$$

A $Y_2Ti_2O_7$ precipitate presenting a cube-on-cube OR with the matrix is presented in Fig. 8(c), whereas smaller precipitates of the same type were also observed, see Fig. 8(d). It has to be noted that the predominant type of precipitates seem to be Y_2O_3 . However, indexation was done on the larger precipitates ($d > 5$ nm), that are more easily detected, whereas the smaller particles ($d < 2$ nm) were more difficult to identify. When assuming that the ratio between $Y_2Ti_2O_7$ and Y_2O_3 is the same for small precipitates and large precipitates, Y_2O_3 would then be the predominant type of precipitates in this sample. It also appears preferentially with a spherical shape.

The precipitates observed and the orientation relationship (OR) found are in agreement with what was previously observed by Ribis and de Carlan [15] in an ODS steel extruded at 1100 °C and then annealed at 1100 °C. Three types of precipitates were detected in this sample:

- (i) $Y_2Ti_2O_7$ pyrochlore-type oxide with a face-centered cubic structure, with a lattice parameter $a = 10.1$ Å;
- (ii) Y_2O_3 with a body-centered cubic structure, with a lattice parameter $a = 10.6$ Å;

- (iii) Y_2O_3 with a face-centered cubic structure, with a lattice parameter $a = 5.2$ Å. Note that the $Y_2Ti_2O_7$ cell is twice larger than the fcc Y_2O_3 cell.

3.2. Atom-probe tomography (APT)

The reconstruction volume of the tip from SPS 850 °C is given in Fig. 9. There is no major clustering of yttrium atoms whereas titanium atoms have clearly diffused to form clusters. Also, a 'coarse' titanium oxide was detected with an equivalent diameter of 43 nm. This is not surprising, given that numerous titanium oxides were detected at grain boundaries and within the bulk of ODS steels SPSed at 850 °C.

Then, there is a much higher tendency of yttrium and oxygen atoms clustering in the ODS steel SPSed at 1100 °C. In Fig. 10, not only Ti and TiO ions but also Y and YO ions are seen in the nanoclusters. This demonstrates that yttrium diffusion is indeed lower than that of titanium and oxygen and most likely constitutes the diffusion limiting species for the formation of oxides.

This first analysis pointed out the presence of yttrium, titanium and oxygen in the clusters (Fig. 10). Then, a "nanocluster analysis" was performed on the two tips in order to study the composition and the size of the nanoparticles. This was done using the 'maximum separation algorithm'. This consists in detecting particles or clusters within the matrix by an algorithm governed by clustering parameters, which were chosen after C. Williams [35]:

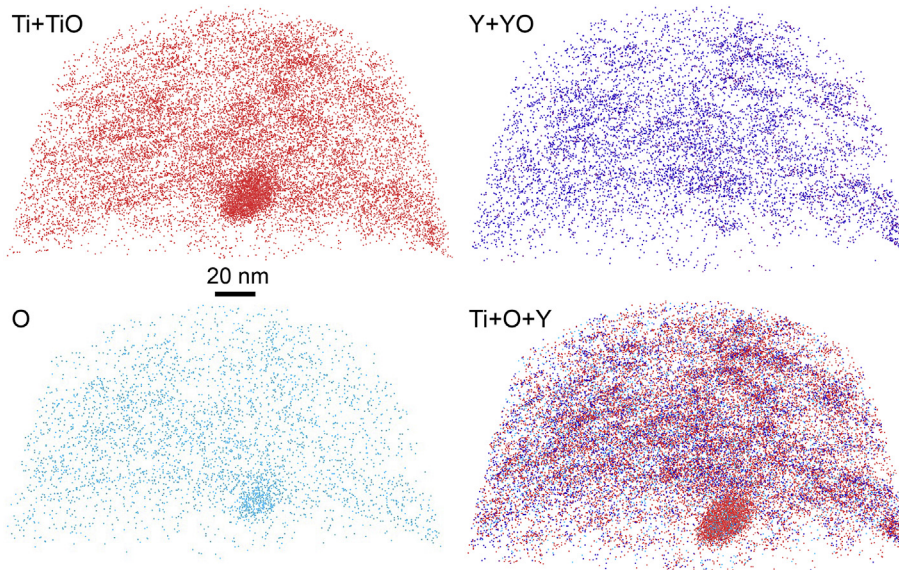


Fig. 9. Reconstruction volume of the tip milled from the sample SPS 850 °C.

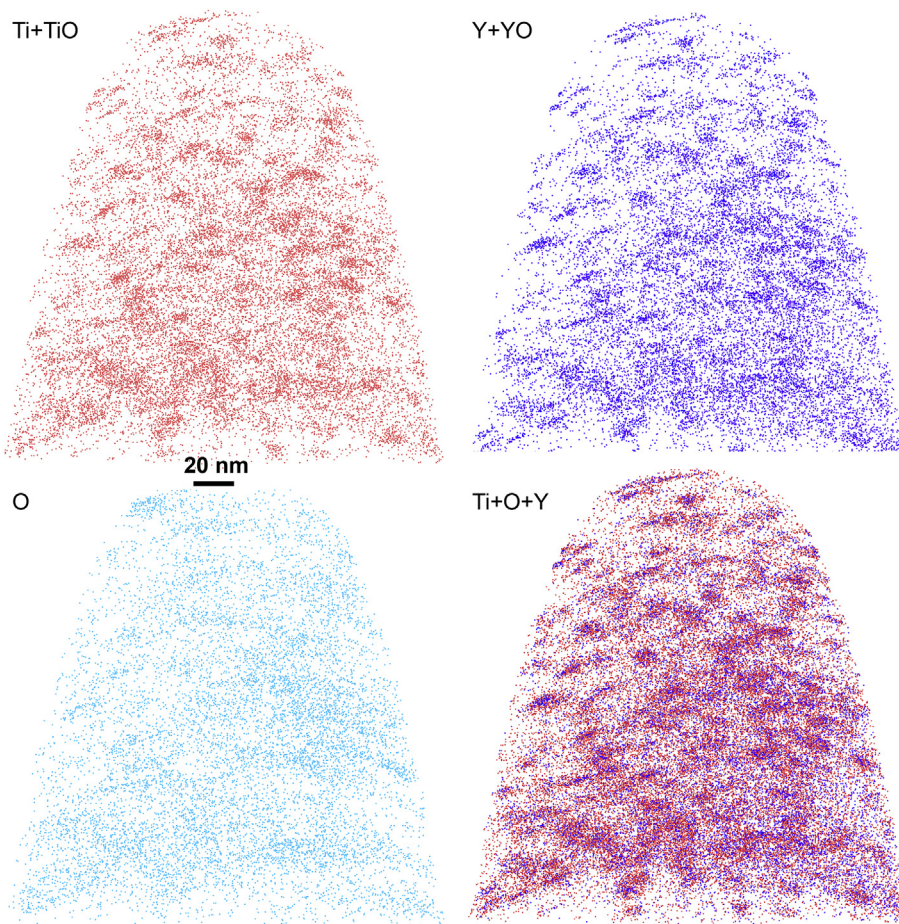


Fig. 10. Reconstruction volume of the tip milled from the sample SPS 1100 °C.

$$\begin{cases} D_{\max} = 0.6 \text{ nm} \\ N_{\min} = 8 \end{cases} \quad (6)$$

D_{\max} is the maximum distance between two atoms within a

cluster and N_{\min} is the minimum number of atoms in a cluster. A complete description of this method can be found in Ref. [35]. The cluster analysis (CA) gives the number density of the detected clusters with the associated composition and size. The mean radius

and number density from APT are 0.7 nm and $1.8 \cdot 10^{24} \text{ m}^{-2}$ in SPS 850 °C and 0.7 nm and $3.7 \cdot 10^{24} \text{ m}^{-2}$ in SPS 1100 °C. The mean radius is twice lower than that from TEM and SANS. Few reasons can explain this difference. First, the results from the CA are more sensitive to subnanometric clusters compared to TEM, which can explain this discrepancy. Indeed, the precipitates visible in TEM already present a crystallographic contrast, whereas the smaller ones might not be completely crystalline. Also, there is a large difference in the probed volume between APT and TEM, and at higher extent between APT and SANS.

More relevant is the composition of the solid solution after extracting the clusters from the matrix (Table 2). The small content of yttrium remaining in solid solution is consistent with the onset of precipitation during consolidation. The amount of oxygen is still high and may come from either contamination during consolidation or from the APT data treating (segregation at grain boundaries or potential coarse oxides not extracted out from the measurement).

4. Numerical study

4.1. Modeling approach

The path to model the precipitation of a second phase within a host phase from a supersaturated solid solution of given solutes (here yttrium, oxygen, titanium) comprises the calculation of:

- (i) the nucleation rate dN/dt at which particles form;
- (ii) the growth rate dR/dt of the nucleated particles;
- (iii) the coarsening kinetics during which the larger precipitates grow at the expense of the smaller ones that dissolve.

These calculations were made step-by-step by solving the classic nucleation, growth, coarsening equations that are fully detailed in Ref. [36].

4.1.1. Nucleation

In the case of spherical particles, this competition between the volume energy against interface energy is illustrated by the following equation:

$$\Delta g_{tot} = \frac{4}{3} \pi R^3 (\Delta g_{ch} + \Delta g_{el}) + 4 \pi R^2 \gamma \quad (7)$$

The volume energy is thus defined by two components: the chemical driving force Δg_{ch} and the elastic energy Δg_{el} .

Then, the nucleation critical radius that allows the Gibbs free energy to be maximized, thus above which the nucleus will be stable, is given by:

$$\frac{d\Delta G(R)}{dR} \Big|_{R=R^*} = 4\pi R^{*2} (\Delta g_{ch} + \Delta g_{el}) + 8\pi R^* \gamma = 0 \quad (8)$$

Which gives R^* :

$$R^* = \frac{-2\gamma}{(\Delta g_{ch} + \Delta g_{el})} \quad (9)$$

Table 2

Composition (at%) of yttrium, titanium and oxygen from APT measurement. Calculations were made by removing the particles using the maximum separation method.

Sample	Yttrium	Titanium	Oxygen
SPS 850 °C	0.09	0.21	0.22
SPS 1100 °C	0.06	0.16	0.21

Once R^* is known, one can derive the thermodynamic barrier for nucleation:

$$\Delta G^* = \Delta G \Big|_{R=R^*} = \frac{16}{3} \pi \frac{\gamma^3}{(\Delta g_{ch} + \Delta g_{el})^2} \quad (10)$$

The chemical driving force Δg_{ch} can be calculated from the solid solution supersaturation s , which quantifies the excess of the solute elements compared to the amount needed to form the precipitates at the equilibrium. For a given precipitate, for instance $\text{Y}_2\text{Ti}_2\text{O}_7$, the supersaturation s is given for a diluted regular solution by:

$$s = \ln \left(\frac{X_Y^2 X_{Ti}^2 X_O^7}{X_Y^{eq2} X_{Ti}^{eq2} X_O^{eq7}} \right) \quad (11)$$

The driving force is logically proportional to this distance from equilibrium:

$$\Delta g_{ch} = \frac{-k_B T}{V_{mol}^p} \cdot s = \frac{-k_B T}{V_{mol}^p} \cdot \ln \left(\frac{X_Y^2 X_{Ti}^2 X_O^7}{X_Y^{eq2} X_{Ti}^{eq2} X_O^{eq7}} \right) \quad (12)$$

V_{mol}^p is the molar volume of the precipitate, k_B the Boltzmann constant, T the temperature. $K_s = X_Y^{eq2} X_{Ti}^{eq2} X_O^{eq7}$ defining the equilibrium is called the solubility product and is assumed to follow this form:

$$\log_{10}(K_s) = \frac{1}{\ln(10)} \times \left(\frac{\Delta H_f - T \Delta S}{k_B T} \right) = \frac{A}{T} + B \quad (13)$$

K_s can be interpreted as the solubility limit of one element extrapolated at n dimensions, n being the number of species forming the precipitate. A and B are well known for nitrides [23], carbides [37,38] and carbonitrides [24] in steels [39] or silicates in Aluminum alloys [40,41]. At the opposite, the value of K_s for oxides in steels is debatable.

The influence of elastic energy is not taken into account in this article, thus we assume $\Delta g_{el} = 0$.

Once ΔG^* and R^* are known, the nucleation rate is given by the Kampmann and Wagner's equation [42]:

$$\frac{dN}{dt} = N_0 Z \beta^* \exp \left(\frac{-\Delta G^*}{k_B T} \right) \cdot f(t, \tau) \quad (14)$$

N_0 is the number of nucleation sites available for the nuclei. If the precipitation is homogeneous and occurs wherever in the material, then $N_0 = 1/V_{at}^m$ where V_{at}^m is the atomic volume of the matrix ($N_0 = 8.3 \times 10^{28} \text{ m}^{-3}$ in ferrite). However, in industrial alloys where numerous defects can constitute preferential sites for precipitates, N_0 is lower and is governed by the number of particular defects: dislocations [43], grain boundaries or existing second-phase particles like dispersoids [44]. In this case, the nucleation is referred as heterogeneous. Heterogeneous nucleation is the most realistic phenomenon that not only fits solid-state precipitation, but also most of physical phenomenon (see for instance rain in clouds [45] or bubbles in a glass of champagne or mineral water).

β^* is the frequency at which atoms can migrate from interstitial position to another and equals to [36,46]:

$$\beta^* = \frac{4\pi R^{*2}}{a^4} \left(\sum_i \frac{X_i^p}{D_i X_i} \right)^{-1} \quad (15)$$

where a is the lattice parameter, X_i^p the atomic fraction in the precipitate, D_i the diffusion coefficient in the matrix and X_i the atomic fraction in solid solution of the species i . The expression of β^* is sometimes simplified and only the diffusion coefficient of the

slowest element is taken into account. This simplification was used for precipitation of Y_2O_3 where yttrium was limitant for nucleation [47]:

$$\beta^* \approx \frac{4\pi R^{*2}}{a^4} \frac{D_Y X_Y}{X_Y^p} \quad (16)$$

The incubation time function $f(t, \tau)$ varies in the literature. In the present model, $f(t, \tau) = 1 - \exp(-t/\tau)$ was used since it matches atomistic models for precipitation of carbonitrides in steels [23]. τ is the incubation time and is given by Ref. $\tau = 2/(\pi\beta Z^2)$ [46].

Z is the Zeldovitch factor, which is given for the case of spherical particles by

$$Z = \frac{V_{mol}^p}{2\pi R^{*2}} \sqrt{\frac{\gamma}{k_B T}} \quad (17)$$

where V_{mol} is the molar volume of the precipitate.

4.1.2. Growth and coarsening

The growth of nucleated particles is then governed by diffusion. Like nucleation, diffusion-governed growth and coarsening are thermally activated. The temperature dependence is traduced by the diffusion coefficient that follows the Arrhenius law:

$$D_i(T) = D_i^0 \times \exp\left(\frac{-Q_i}{R_g T}\right) \quad (18)$$

where D_i^0 is the pre-exponential factor in $m^2 \cdot s^{-1}$, Q_i the activation energy in $J \cdot mol^{-1}$, $R_g = 8.314 J \cdot K^{-1} \cdot mol^{-1}$ the gas constant and T the temperature in K.

For spherical particles of radii R of composition $Y_2Ti_2O_7$:

$$\begin{cases} \frac{dR}{dt} = \frac{D_Y}{R} \frac{X_Y^m - X_Y^i(R)}{\alpha X_Y^p - X_Y^i(R)} \\ \frac{dR}{dt} = \frac{D_{Ti}}{R} \frac{X_{Ti}^m - X_{Ti}^i(R)}{\alpha X_{Ti}^p - X_{Ti}^i(R)} \\ \frac{dR}{dt} = \frac{D_O}{R} \frac{X_O^m - X_O^i(R)}{\alpha X_O^p - X_O^i(R)} \end{cases} \quad (19)$$

where α is the ratio between the atomic volume of the matrix V_{at}^m and of the precipitate V_{at}^p . D_Y , X_Y^m , X_Y^p and $X_Y^i(R)$ are the diffusion coefficient of yttrium in α -iron, the atomic fraction of yttrium in solid solution, in the precipitate and at the interface, the latter being dependent of the radius R .

Indeed, the solubility product is modified by the curvature of the precipitate and thus depends on the precipitate radius. The solubility in the presence of small particles with a large ratio of surface area to volume is larger than that for larger ones [42]. This is due to the minimization of the interfacial energy that is actually higher for smaller precipitates. This size-dependence is called the Gibbs–Thomson effect and is traduced for the case of $Y_2Ti_2O_7$ by equation (20) [48]:

$$X_Y^i(R) X_{Ti}^i(R) X_O^i(R) = K_s \cdot \exp\left(\frac{2\gamma V_{mol}^p}{R_g k_B T}\right) \quad (20)$$

This gives rise to coarsening, which is traduced by a general increase in the mean radius when smaller particles are diluted into the larger ones. During this process also commonly referred to as Ostwald ripening, the precipitate number density can be reduced from Ref. $\approx 10^{25} m^{-3}$ to less than $10^{19} m^{-3}$ in

typical two-phase alloys during aging [42]. Even if the coarsening process is considered to be confined to the latest stages of precipitation, it may accompany the growth process or may even start while the system is still in its nucleation period, depending on the initial supersaturation of the solid solution.

4.2. Numerical results

4.2.1. Calibrating the model

Four parameters are used in this model: A and B for the solubility product, the interfacial energy γ and finally the coefficient diffusion of yttrium in ferrite D_Y . The key-parameters used for the simulations are given in Table 3.

Specially, the yttrium coefficient not only governs the nucleation onset but also determines the growth rate. Indeed, since it is the slowest solute element in the precipitate compared to titanium and oxygen, it will regulate the diffusion from the matrix into the precipitate. The 'calculated' diffusion coefficient of yttrium in α -iron suggested that yttrium diffused 400 times lower than iron self-diffusion at 850 °C [17], which confirmed the role of yttrium as diffusion-limiting species for the precipitation process. There is no reliable direct experimental measurement of yttrium coefficient diffusion in either ferrite or austenite, which makes the coefficient after [17] a unique value to work with [15]. An alternative expression was determined by Murali et al. [49] by density functional theory (DFT). The diffusion coefficient determined by Hin was fitted with experimental data in a limited temperature range, up to 1150 °C. This was indeed restricted to the range of typical consolidation temperatures of ODS steels. However, all recent studies prove that the coarsening behavior of Y_2O_3 and more importantly $Y_2Ti_2O_7$ is observed at higher temperature, typically 1200 °C, 1300 °C and 1400 °C. Consequently, if the diffusion coefficient accurately reproduces the precipitation kinetics of Y_2O_3 during consolidation, it seems to overestimate the diffusivity of yttrium at higher temperature. This induces a much too high coarsening rate compared to that calculated from the aforementioned studies at very high temperatures. As a consequence, a new expression of the diffusion coefficient is proposed:

$$D_Y = 10^{-7} \exp\left(\frac{-260 [kJ/mol]}{R_g T}\right) \quad (21)$$

The pre-exponential factor was decreased so that the diffusion of yttrium was retarded and so was the nucleation. Also, the growth rate of precipitates was proportionally decreased. In the same manner, the activation energy was decreased down to 260 $kJ \cdot mol^{-1}$ instead of 320 $kJ \cdot mol^{-1}$, thus the temperature dependency of the diffusion mechanism (the slope in the Arrhenius' plot) was decreased. The present value is equal to that from Hin at low temperatures but significantly deviates into lower values at high temperatures. At 1300 °C, 1.2×10^{-15} for the former value versus 2.3×10^{-16} for the new value.

4.2.2. Precipitation of Y_2O_3

Since $Y_2Ti_2O_7$ are known to preferentially form in steels containing titanium, only Ti-free ODS steels were considered to model the precipitation behavior of Y_2O_3 . The ODS steels with published experimental nanoscale characterization that were used for this study are summarized in Table 4. In order to compare to the precipitation state of ODS steels produced by HIPing or extrusion, non-isothermal treatments were simulated at the possible consolidation temperatures (850, 1000, 1100 °C).

Table 3

Thermodynamic and diffusion parameters used for the precipitation model of Y_2O_3 and $Y_2Ti_2O_7$. In red color are the fitted parameters. (For interpretation of the references to colour in this figure legend, the reader is referred to the web version of this article.)

Parameter	Value	Value source	Source
bcc ferrite			
lattice parameter	$a = 2.886 \times 10^{-10} \text{ m}$		[This work]
atomic volume	$v_{at}^{\alpha} = 1.202 \times 10^{-29} \text{ m}^3$		
diffusion coeff.	$D^0 [\text{m}^2 \cdot \text{s}^{-1}]$	$Q [\text{kJ} \cdot \text{mol}^{-1}]$	
Yttrium	1×10^{-5}	299	[18]
Yttrium	1×10^{-7}	260	[This work]
titanium	0.21	293	[50]
oxygen	3×10^{-5}	139	[51,52]
bcc Y_2O_3			
atomic volume	$v_{at}^{Y_2O_3} = 1.49 \times 10^{-29} \text{ m}^3$		[This work]
solubility product	$\log(K_S) = \frac{-20000}{T} - 4$		
interfacial energy	$\gamma^{Y_2O_3} = 0.35 \text{ J} \cdot \text{m}^{-2}$		TEM [15]
	$\gamma^{Y_2O_3} = 0.60 \text{ J} \cdot \text{m}^{-2}$		[This work]
Pyrochlore type $Y_2Ti_2O_7$			
atomic volume	$v_{at}^{Y_2Ti_2O_7} = 9.9 \times 10^{-30} \text{ m}^3$		[This work]
solubility product	$\log(K_S) = \frac{-19000}{T} - 25$		
interfacial energy	$\gamma^{Y_2Ti_2O_7} = 0.25 \text{ J} \cdot \text{m}^{-2}$		TEM [15]
	$\gamma^{Y_2Ti_2O_7} = 0.48 \text{ J} \cdot \text{m}^{-2}$		[This work]

Table 4

Composition of Y, Ti and O, treatments and resulting precipitate states of Ti-free ODS steels used for comparison with the numerical results.

	Cr	Y	O	Ti	Treatment	R_m [nm]	N_p [m^{-3}]	Ref.
(wt%/at%)	18/19.2	0.24/0.15	0.06/0.22	0	850 °C - 1 h	1.5	9.1×10^{23}	[53]
					1100 °C - 1 h	6	9.0×10^{21}	
(wt%/at%)	13.9/15	0.21/0.13	0.05/0.18	0	HIP 850 °C - 3 h	1.43	1.1×10^{24}	[29]
					HIP 1100 °C - 3 h	5.39	7.9×10^{21}	

Fig. 11 describes the temporal evolution of the mean radius and the number density of Y_2O_3 during non-isothermal treatments simulating the HIP process usually made on the milled powder with composition recalled in Table 4. The HIP cycle chosen here consists of a heating at $20 \text{ K} \cdot \text{min}^{-1}$ up to the consolidation temperature and then a soaking stage of 3 h [29]. In order to illustrate the influence of the interfacial energy on the precipitation, the figure reports the precipitation kinetics with four different interfacial energies, from 0.3 to $0.6 \text{ J} \cdot \text{m}^{-2}$. Within the temperature range, the nucleation of Y_2O_3 is rapidly achieved, mainly during the heating stage of the HIP cycle. Then, the mean radius increases whereas the number density decreases, which corresponds to the coarsening stage. Based on these results, the nucleation of Y_2O_3 seems to be completed before that the maximum temperature is reached. Thus, coarsening occurs early during the consolidation at the maximum temperature, from 850 °C to 1150 °C. The mean radius of Y_2O_3 after HIP is well reproduced at 850 °C but slightly differs from SANS results at 1000 and 1100 °C since the simulated mean radius is overestimated.

Fig. 12 describes the temporal evolution of the simulated mean radius and number density of Y_2O_3 and the comparison of published experimental data of the same composition from Ratti et al. [54]. The simulation also reproduces consistent results at 850 °C but slightly underestimates the mean radius observed by SANS at 1100 °C. Since at 1000 °C and 1100 °C the mean radius of Y_2O_3 after Alinger and Hin is at the contrary overestimated, one can conclude that there is no biased tendency of the model to underestimate/overestimate the coarsening behavior of Y_2O_3 . Instead, the numerical results are in very good agreement with the experimental data from SANS. The interfacial energy giving rise to the best match between experiments and simulations is $\gamma^{Y_2O_3} = 0.6 \text{ J} \cdot \text{m}^{-2}$, which is higher than those from either Hin ($0.4 \text{ J} \cdot \text{m}^{-2}$) or Ribis ($0.35 \text{ J} \cdot \text{m}^{-2}$) but this is still consistent with semi-coherent particles. However,

the interfacial energy used in this study can be considered as the parameter that takes into account any evolution in morphology, misfit energy and relationship effect of the precipitates with regards to the matrix. As such, the absolute value cannot be directly compared to assumed experimental value or purely thermodynamic calculation.

4.2.3. Precipitation of $Y_2Ti_2O_7$

The simulated precipitation behavior of $Y_2Ti_2O_7$ during HIPing is represented in Fig. 13. The kinetics is quite similar to that of Y_2O_3 since it is governed by the diffusion of yttrium (Fig. 11). The main difference is the higher number density for $Y_2Ti_2O_7$ compared to Y_2O_3 , which can be explained by the larger solute content available for the precipitation of $Y_2Ti_2O_7$ (see Table 5).

Also, the thermal stability of the oxides was assessed using the model. The annealing treatments were taken from Miao et al. [55] who performed annealing treatments for very long time (3000 h) on an extruded ferritic steel. Fig. 14 reports the precipitation behavior during successive hot extrusion and annealing at either 900, 950 or 1000 °C for 3000 h. At long annealing treatments, the model slightly anticipates the coarsening stage compared to what was observed by Miao et al.

In order to assess the model for rapid non-isothermal treatments, the present model was applied to the precipitation kinetics during SPS consolidation. Fig. 15 shows the comparison between experimental data collected by SANS, ATP and TEM and numerical data from the model. Given the scattered experimental data of the mean radius and the number density, the numerical results are acceptable. However, it seems to accentuate the effect of the temperature on the coarsening behavior because the difference in the number density between SPS850 °C and SPS1100 °C is higher than that observed experimentally.

The Gibbs–Thomson effect was applied assuming a spherical shape of the precipitates, which may not be fully accurate. Indeed,

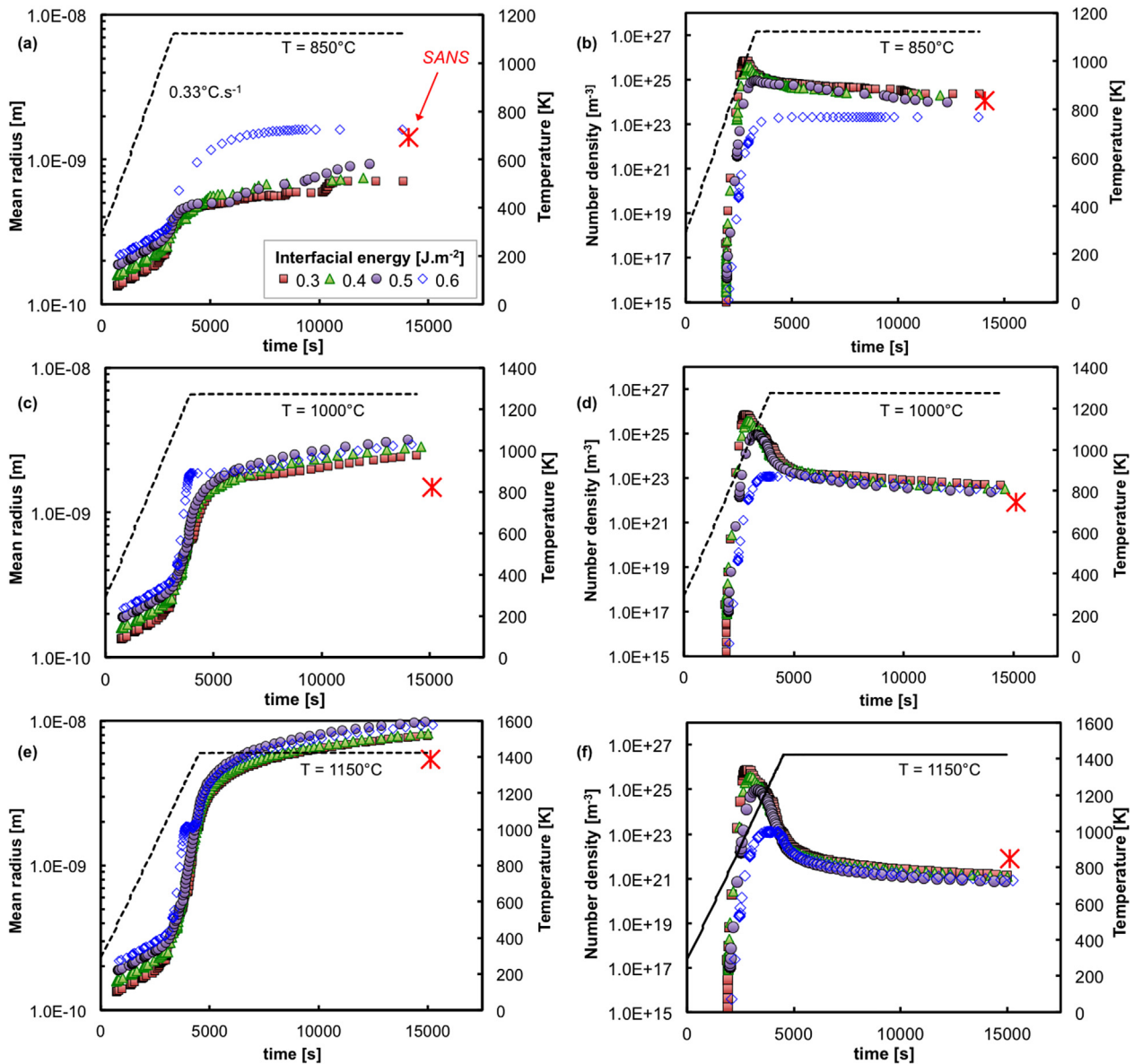


Fig. 11. Time evolution (linear scale) of simulated mean radius and number density of Y_2O_3 particles during non-isothermal HIPing at (a–b) 850 °C, (c–d) 1000 °C, (e–f) 1100 °C. SANS data from Alinger et al. [29,30] and [47].

Ribis showed that a deviation from spherical into ellipsoidal or cuboidal shape occurred upon annealing at high temperature, which was even confirmed during rapid consolidation by the present study. In this context, the coarsening kinetics would be impacted, which may explain the difference in coarsening kinetics between experimental and numerical results.

5. Conclusions

The precipitation kinetics of Y_2O_3 and $\text{Y}_2\text{Ti}_2\text{O}_7$ from a supersaturated solid solution of yttrium, oxygen and titanium during non-isothermal treatments similar to industrial high-temperature consolidation was simulated. Despite of strong assumptions (homogeneous nucleation, stoichiometric phases, etc), the model gave rise to interesting results. Since the driving force is dependent on the level of saturation in the solid solution (chemical composition), the readership must keep in mind that the present results are not directly applicable to any alloy and further calculations must be

made with the proper chemical composition and the suitable thermal treatment.

A new expression of the diffusion coefficient of yttrium in ferrite was proposed. First, the nucleation was achieved during the heating stage of the non-isothermal treatment, nearly 600 °C. This early nucleation is in very good agreement with the literature and with the actual precipitation state within the ODS SPSed in a few minutes at 850 °C and 1100 °C. The simulations reproduce the precipitation kinetics during non-isothermal treatments in the temperature range of typical consolidation cycles (from 850 °C to 1100 °C).

The model also predicts the thermal stability of Y_2O_3 and $\text{Y}_2\text{Ti}_2\text{O}_7$ but seems to overestimates the coarsening stage compared to the published experimental data. The number density from the simulation is higher than that measured on SPSed ODS steels. This can be explained by the assumption of a unique and stoichiometric phase in the simulation whereas in the reality the particles may observe variation in the composition, not only in yttrium, titanium

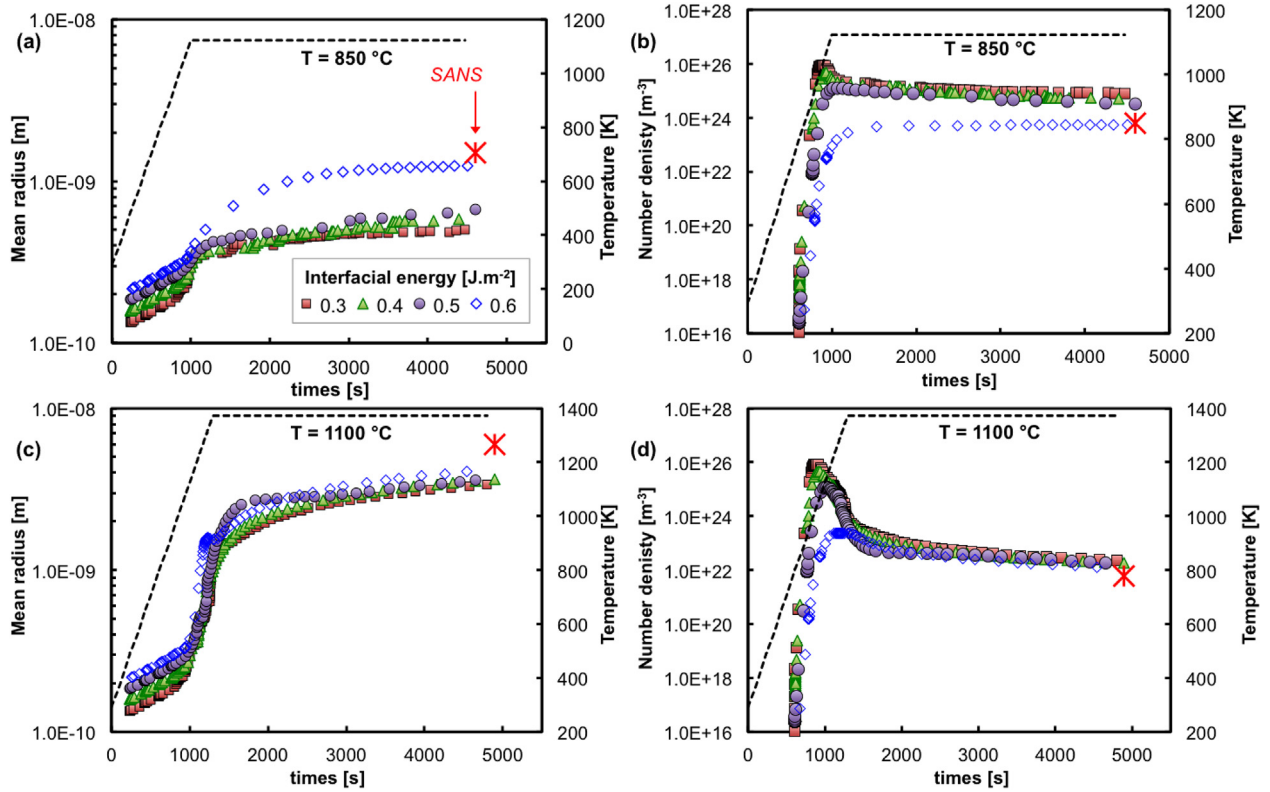


Fig. 12. Time evolution (linear scale) of simulated Mean radius and number density of Y_2O_3 particles during non-isothermal pressure-free heat treatments at (a–b) 850 °C and (c–d) 1100 °C. SANS data are from Ratti et al. [53,54].

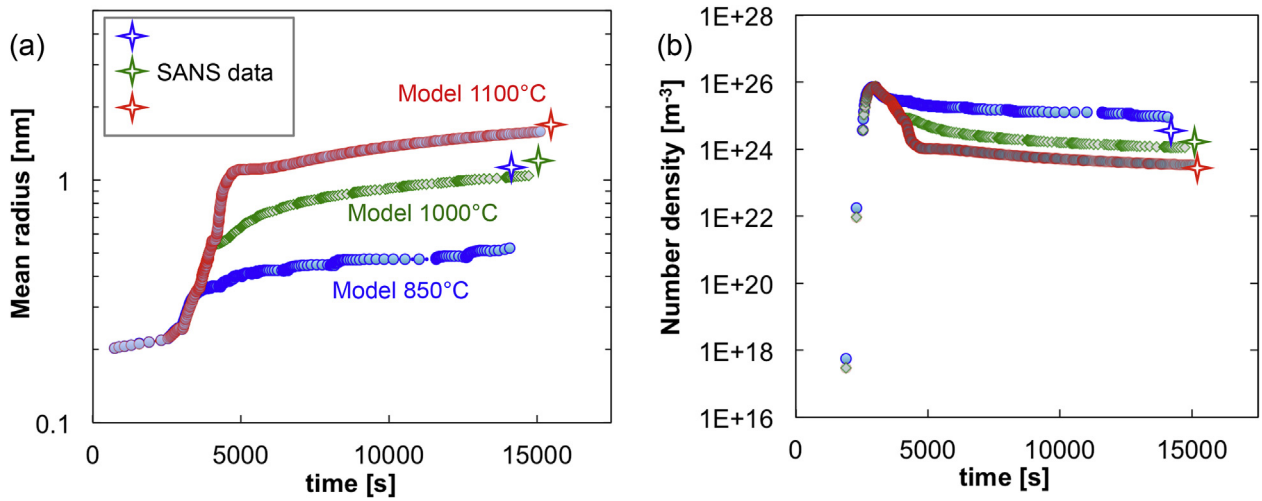


Fig. 13. Time evolution (linear scale) of simulated Mean Radius and Number Density of $Y_2Ti_2O_7$ particles during non-isothermal heat treatments at (a–b) 850 °C, 1000 °C and 1100 °C. SANS data are from Alinger et al. [29,30].

Table 5

Composition of Y, Ti and O, heat treatments and resulting precipitate states of ODS steels used for comparison with the numerical results.

	Cr	Y	O	Ti	Treatment	R_m [nm]	N_p [m^{-3}]	Ref.
(wt%/at%)	13.9/15	0.21/0.13	0.05/0.18	0.4/0.4	HIP 850 °C - 3 h	1.25	2.57×10^{24}	[29]
					HIP 1000 °C - 3 h	1.53	8.5×10^{23}	
					HIP 1100 °C - 3 h	1.71	3.02×10^{23}	

and oxygen but also in the enrichment in other solutes like aluminum, silicon or chromium. The latter has been located in

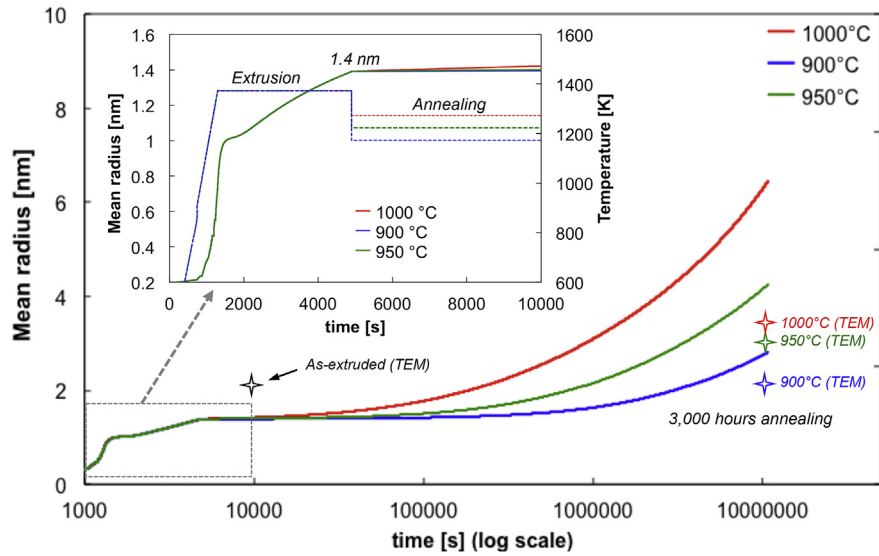


Fig. 14. Time evolution of simulated Mean radius and Number Density of $Y_2Ti_2O_7$ particles. The inset focuses on the mean radius evolution during extrusion. Experimental values after [55].

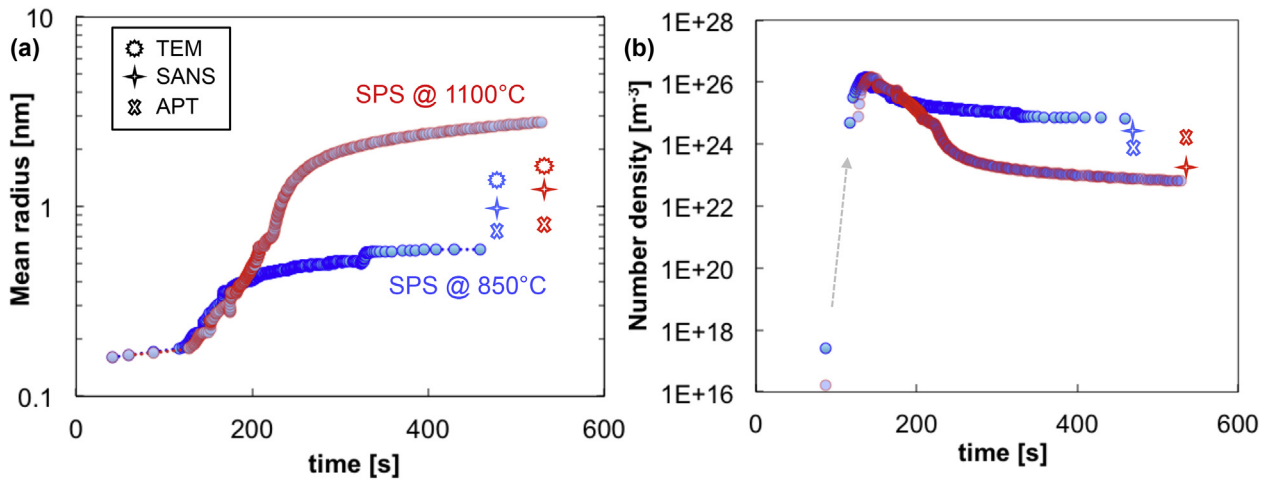


Fig. 15. Time evolution of simulated Mean radius and Number Density of $Y_2Ti_2O_7$ particles compared to experimental data from TEM (circle), SANS (star) and APT (cross).

nanosized particles [56] or under the form of a shell surrounding the particles [8]. This deviation is probably emphasized in SPSed ODS steels compared to HIPed materials because SPS gives rise to very rapid treatments during which particles may have no time to reach their equilibrium state. Hence, the assumption of stoichiometric particles instead of probable far-from-equilibrium nanoclusters is most likely not applicable. Also, the excess vacancies were neglected, in terms of both diffusion and atomic volume of the 'compound'. The latter have been reported to play a role on the nanoparticles stability [14]. Most importantly, the effect of morphological change upon heating was not taken into account in the present model. The modification of the Gibbs–Thomson effect due to morphological variations on their effect on the coarsening kinetics will be discussed in a future article.

Acknowledgments

X. B. was supported by the European Community (269706) within the Project MATTER. Thanks are due to the CLYM (Centre Lyonnais de Microscopie) in Lyon for access to the microscope.

Thanks are also due to M. Descoins, M. Houmada and D. Manginck for performing the atom-probe primary analyses.

References

- [1] R. Klueh, D. Gelles, S. Jitsukawa, A. Kimura, G.R. Odette, B. van der Schaaf, Ferritic/martensitic steels – overview of recent results, *J. Nucl. Mater.* 307–311 (2002) 455–465 (Part 1).
- [2] Y. de Carlan, J.-L. Bechade, P. Dubuisson, J.-L. Seran, P. Billot, A. Bougault, T. Cozzika, S. Doriot, D. Hamonand, J. Henry, M. Ratti, N. Lochet, D. Nunes, P. Olier, T. Leblond, M. Mathon, CEA developments of new ferritic ODS alloys for nuclear applications, *J. Nucl. Mater.* 386–388 (2009) 430–432.
- [3] S. Saroja, A. Dasgupta, R. Divakar, S. Raju, E. Mohandas, M. Vijayalakshmi, K.B.S. Rao, B. Raj, Development and characterization of advanced 9Cr ferritic/martensitic steels for fission and fusion reactors, in: *Proceedings of the IAEA-ec Topical Meeting on Development of New Structural Materials for Advanced Fission and Fusion Reactor Materials*, Journal of Nuclear Materials, Vol. 409, 2011, pp. 131–139.
- [4] M. Auger, V. de Castro, T. Leguey, A. Muñoz, R. Pareja, Microstructure and mechanical behavior of ODS and non-ODS Fe–14Cr model alloys produced by spark plasma sintering, *J. Nucl. Mater.* 436 (2013) 68–75.
- [5] X. Boulnat, D. Fabrègue, M. Perez, M.-H. Mathon, Y. de Carlan, High-temperature tensile properties of nano-oxide dispersion strengthened ferritic steels produced by mechanical alloying and spark plasma sintering, *Metall. Mater. Trans. A* 44 (6) (2013) 2461–2465.

- [6] C. Cayron, A. Montani, D. Venet, Y. de Carlan, Identification of new phases in annealed Fe–18CrWTi ODS powders, *J. Nucl. Mater.* 399 (2–3) (2010) 219–224.
- [7] Y. Wu, E. Haney, N. Cunningham, G. Odette, Transmission electron microscopy characterization of the nanostructures in nanostructured ferritic alloy MA957, *Acta Mater.* 60 (8) (2012) 3456–3468.
- [8] V. de Castro, E. Marquis, S. Lozano-Perez, R. Pareja, M.L. Jenkins, Stability of nanoscale secondary phases in an oxide dispersion strengthened Fe–12Cr alloy, *Acta Mater.* 59 (10) (2011) 3927–3936.
- [9] X. Boulnat, M. Perez, D. Fabrègue, T. Douillard, M.-H. Mathon, Y. de Carlan, Microstructure evolution in nano-reinforced ferritic steel processed by mechanical alloying and spark plasma sintering, *Metall. Mater. Trans. A* 45A (2014) 1485–1497.
- [10] C. Heintze, F. Bergner, A. Ulbricht, M. Hernández-Mayoral, U. Keiderling, R. Lindau, T. Weissgärber, Microstructure of oxide dispersion strengthened eurofer and iron–chromium alloys investigated by means of small-angle neutron scattering and transmission electron microscopy, *J. Nucl. Mater.* 416 (1–2) (2011) 35–39.
- [11] M. Mathon, M. Perrut, S. Zhong, Y. de Carlan, Small angle neutron scattering study of martensitic/ferritic ODS alloys, *Journal of Nuclear Materials* 428 (1–3) (2012) 147–153.
- [12] C.A. Williams, P. Unifantowicz, N. Baluc, G. Smith, E.A. Marquis, The formation and evolution of oxide particles in oxide-dispersion-strengthened ferritic steels during processing, *Acta Mater.* 61 (6) (2013) 2219–2235.
- [13] N. Cunningham, Y. Wu, D. Klingensmith, G. Odette, On the remarkable thermal stability of nanostructured ferritic alloys, *Mater. Sci. Eng. A* 613 (0) (2014) 296–305.
- [14] A. Hirata, T. Fujita, Y.R. Wen, J.H. Schneibel, C.T. Liu, M.W. Chen, Atomic structure of nanoclusters in oxide-dispersion strengthened steels, *Nat. Mater.* 10 (2011) 922–926.
- [15] J. Ribis, Y. de Carlan, Interfacial strained structure and orientation relationships of the nanosized oxide particles deduced from elasticity-driven morphology in oxide dispersion strengthened materials, *Acta Mater.* 60 (1) (2012) 238–252.
- [16] E. Kozeschnik, *Modeling Solid-state Precipitation*, Momentum Press, LLC, New York, 2013.
- [17] C. Hin, B.D. Wirth, J.B. Neaton, Formation of Y_2O_3 nanoclusters in nanostructured ferritic alloys during isothermal and anisothermal heat treatment: A kinetic Monte Carlo study, *Phys. Rev. B* 80 (2009) 134118.
- [18] C. Hin, B. Wirth, Formation of oxide nanoclusters in nanostructured ferritic alloys during anisothermal heat treatment: A kinetic monte carlo study, *Mater. Sci. Eng. A* 528 (4–5) (2011) 2056–2061.
- [19] E. Kozeschnik, J. Svoboda, P. Fratzl, F. Fischer, Modelling of kinetics in multi-component multi-phase systems with spherical precipitates: I: Numerical solution and application, *Mater. Sci. Eng. A* 385 (1–2) (2004) 157–165.
- [20] S. Esmaeili, D. Lloyd, W. Poole, A yield strength model for the Al–Mg–Si–Cu alloy AA6111, *Acta Mater.* 51 (2003) 2243–2257.
- [21] E. Clouet, M. Nastar, C. Sigli, Nucleation of Al_3Zr and Al_3Sc in aluminium alloys: from kinetic Monte Carlo simulations to classical theory, *Phys. Rev. B* 69 (2004) 1–14.
- [22] E. Clouet, A. Barbu, L. Laé, G. Martin, Precipitation kinetics of Al_3Zr and Al_3Sc in aluminium alloys modeled with cluster dynamics, *Acta Mater.* 53 (2005) 2313–2325.
- [23] P. Maugis, M. Gouné, Kinetics of vanadium carbonitride precipitation in steel: A computer model, *Acta Mater.* 53 (12) (2005) 3359–3367.
- [24] M. Perez, E. Courtois, D. Acevedo, T. Epicier, P. Maugis, Precipitation of niobium carbonitrides in ferrite: chemical composition measurements and thermodynamic modelling, *Philos. Mag. Lett.* 87 (9) (2007) 645–656.
- [25] J.M. Torralba, L. Fuentes-Pacheco, N. García-Rodríguez, M. Campos, Development of high performance powder metallurgy steels by high-energy milling, *Adv. Powder Technol.* 24 (5) (2013) 813–817.
- [26] M. Brocq, B. Radiguet, J.-M.L. Breton, F. Cuvilly, P. Pareige, F. Legendre, Nanoscale characterisation and clustering mechanism in an Fe– Y_2O_3 model ODS alloy processed by reactive ball milling and annealing, *Acta Mater.* 58 (5) (2010) 1806–1814.
- [27] M. Laurent-Brocq, F. Legendre, M.-H. Mathon, A. Mascaró, S. Poissonnet, B. Radiguet, P. Pareige, M. Loyer, O. Leseigneur, Influence of ball-milling and annealing conditions on nanocluster characteristics in oxide dispersion strengthened steels, *Acta Mater.* 60 (20) (2012) 7150–7159.
- [28] A. Hirata, T. Fujita, C. Liu, M. Chen, Characterization of oxide nanoprecipitates in an oxide dispersion strengthened 14YWT steel using aberration-corrected STEM, *Acta Mater.* 60 (16) (2012) 5686–5696.
- [29] M.J. Alinger, On the Formation and Stability of Nanometer Scale Precipitates in Ferritic Alloys during Processing and High Temperature Service, University of California Santa Barbara, 2004. Ph.D. thesis.
- [30] M. Alinger, G. Odette, D. Hoelzer, On the role of alloy composition and processing parameters in nanocluster formation and dispersion strengthening in nanostructured ferritic alloys, *Acta Mater.* 57 (2) (2009) 392–406.
- [31] C. Heintze, M. Hernández-Mayoral, A. Ulbricht, F. Bergner, A. Shariq, T. Weissgärber, H. Frielinghaus, Nanoscale characterization of ODS Fe–9%Cr model alloys compacted by spark plasma sintering, *J. Nucl. Mater.* 428 (1–3) (2012) 139–146.
- [32] B. Sonderegger, E. Kozeschnik, Interfacial energy of diffuse phase boundaries in the generalized broken-bond approach, *Metall. Mater. Trans. A* 41A (2010) 3262–3269.
- [33] B. Sonderegger, E. Kozeschnik, Size dependence of the interfacial energy in the generalized nearest-neighbor broken-bond approach, *Scr. Mater.* 60 (8) (2009) 635–638.
- [34] B. Fultz, J.M. Howe, *Transmission Electron Microscopy and Diffractometry of Materials*, Springer Science & Business Media, 2012.
- [35] C.A. Williams, *Atomic Scale Characterisation of Oxide Dispersion Strengthened Steels for Fusion Applications*, University of Oxford, 2011. Ph.D. thesis.
- [36] M. Perez, M. Dumont, D. Acevedo-Reyes, Implementation of classical nucleation and growth theories for precipitation, *Acta Mater.* 56 (9) (2008) 2119–2132.
- [37] F. Perrard, A. Deschamps, P. Maugis, Modelling the precipitation of nbc on dislocations in Refs. *alpha-fe*, *Acta Mater.* 55 (4) (2007) 1255–1266.
- [38] E.J. Pavlina, J.G. Speer, C.J.V. Tyne, Equilibrium solubility products of molybdenum carbide and tungsten carbide in iron, *Scr. Mater.* 66 (5) (2012) 243–246.
- [39] T. Gladman, *The Physical Metallurgy of Microalloyed Steels*, Maney Publishing, 1997.
- [40] G. Fribourg, Y. Bréchet, A. Deschamps, A. Simar, Microstructure-based modelling of isotropic and kinematic strain hardening in a precipitation-hardened aluminium alloy, *Acta Mater.* 59 (2011) 3621–3635.
- [41] D. Bardel, M. Perez, D. Nelias, A. Deschamps, C. Hutchinson, D. Maisonnette, T. Chaise, J. Garnier, F. Bourlier, Coupled precipitation and yield strength modelling for non-isothermal treatments of a 6061 aluminium alloy, *Acta Mater.* 62 (0) (2014) 129–140.
- [42] R. Wagner, R. Kampmann, P.W. Voorhees, *Homogeneous Second-phase Precipitation*, Wiley-VCH Verlag GmbH & Co. KGaA, 2006.
- [43] F. Perrard, A. Deschamps, F. Bley, P. Donnadieu, P. Maugis, A small-angle neutron scattering study of fine-scale NbC precipitation kinetics in the α -Fe–Nb–C system, *J. Appl. Crystallogr.* 39 (4) (2006) 473–482.
- [44] C. Gallais, A. Denquin, Y. Bréchet, G. Lapasset, Precipitation microstructures in an {AA6056} aluminium alloy after friction stir welding: Characterisation and modelling, *Mater. Sci. Eng. A* 496 (1–2) (2008) 77–89.
- [45] H. Pruppacher, J. Klett, *Microphysics of Clouds and Precipitation*, Springer, Ch. (Chapter 9): Heterogeneous nucleation.
- [46] M. Perez, M. Dumont, D. Acevedo-Reyes, Corrigendum to “implementation of classical nucleation and growth theories for precipitation”, *Acta Mater.* 56 (2008) 2119–2132. *Acta Materialia* 57 (4) (2009) 1318.
- [47] C. Hin, B. Wirth, Formation of Y_2O_3 nanoclusters in nano-structured ferritic alloys: Modeling of precipitation kinetics and yield strength, *J. Nucl. Mater.* 402 (1) (2010) 30–37.
- [48] M. Perez, Gibbs–thomson effects in phase transformations, *Scr. Mater.* 52 (8) (2005) 709–712.
- [49] D. Murali, B. Panigrahi, M. Valsakumar, C. Sundar, Diffusion of Y and Ti/Zr in bcc iron: A first principles study, *J. Nucl. Mater.* 419 (1–3) (2011) 208–212.
- [50] P. Klugkist, C. Herzig, Tracer diffusion of titanium in α -iron, *Phys. status solidi* 148 (1995) 413–421.
- [51] R. Barlow, P.J. Grundy, The determination of the diffusion constants of oxygen in nickel and α -iron by an internal oxidation method, *J. Mater. Sci.* 4 (1969) 797–801.
- [52] J. Takada, M. Adachi, Determination of diffusion coefficient of oxygen in α -iron from internal oxidation measurements in Fe–Si alloys, *J. Mater. Sci.* 21 (1986) 2133–2137.
- [53] M. Ratti, D. Leuvrey, M. Mathon, Y. de Carlan, Influence of titanium on nanocluster (Y, Ti, O) stability in ODS ferritic materials, *J. Nucl. Mater.* 386–388 (0) (2009) 540–543.
- [54] M. Ratti, Development of new ferritic/martensitic steels for RNR–Na tube cladding materials, translated from ‘Développement de nouvelles nuances d’aciers ferritiques/martensitiques pour le gainage d’éléments combustibles des Réacteurs à Neutrons Rapides au sodium’, Institut Polytechnique de Grenoble, 2010. Ph.D. thesis.
- [55] P. Miao, G. Odette, T. Yamamoto, M. Alinger, D. Klingensmith, Thermal stability of nano-structured ferritic alloy, *J. Nucl. Mater.* 377 (2008) 59–64.
- [56] M. Miller, D. Hoelzer, E. Kenik, K. Russell, Nanometer scale precipitation in ferritic MA/ODS alloy MA957, *J. Nucl. Mater.* 329–333 (0) (2004) 338–341. Part A.